Volume 1 | Number 1 | Jan 2013 | Pages 1–100

Journal of
Materials Chemistry C

Materials for optical and electronic devices
www.rsc.org/materialsC

ROYAL SOCIETY
OF CHEMISTRY

ROYAL SOCIETY
OF CHEMISTRY

www.rsc.org/materialsC

Substitution of Silicon Within the Rhombohedral Boron Carbide (B$_4$C) Crystal Lattice Through High-Energy Ball-Milling

Manoj K. Kolel-Veetil[a]*, Raymond M. Gamache[a], Noam L. Bernstein[b], Ramasis Goswami[b], Syed B. Qadri[b], Kenan P. Fears[a], Joel B. Miller[a], Evan R. Glaser[c] and Teddy M. Keller[a]

[a]Chemistry Division, [b]Materials Sciences Division and [c]Electronic Science & Technology Division, Naval Research Laboratory, Washington, DC 20375.

Corresponding Author

*Manoj Kolel-Veetil (Manoj.kolel-veetil@nrl.navy.mil)

ABSTRACT Boron carbide (B_4C) is a ceramic with a structure composed of B_{12} or $B_{11}C$ icosahedra bonded to each other and to three(C and/or B)-atom chains. Despite its excellent hardness, B_4C fails catastrophically under shock loading, but substituting other elements into lattice sites may change and possibly improve its mechanical properties. Density functional theory calculations of elemental inclusions in the most abundant polytypes of boron carbide, B_{12}-CCC, B_{12}-CBC, and $B_{11}C^p$-CBC, predict that the preferential substitution site for metallic elements (Be, Mg and Al) is the center atom and that for non-metallic elements (N, P and S) it is generally the end of the three-atom chain in B_4C's rhombohedral crystal lattice. However, Si, a semi-metal, seems to prefer the chain center in B_{12}-CCC and icosahedral polar sites in both B_{12}-CBC and $B_{11}C^p$-CBC. As a first step to testing the feasibility of elemental substitutions experimentally, Si atoms were incorporated into B_4C at low temperatures (~200-400 ^{o}C) by high-energy ball-milling. High-resolution transmission electron microscopy showed that the Si atoms were uniformly dispersed in the product, and the magnitude of the lattice expansion and Rietveld analysis of the X-ray diffraction data were analyzed to determine the likely sites of Si substitution in B_4C. Further corroborative evidence was obtained from electron spin resonance spectroscopy, magic-angle spinning nuclear magnetic resonance spectroscopy, X-ray photoelectron spectroscopy and Raman spectroscopy characterizations of the samples. Thus, a simple, top-down approach to manipulating the chemistry of B_4C is presented with potential for generating materials with tailored properties for a broad range of applications.

Introduction

Boron carbide with the chemical formula B_4C is a ceramic material with many useful properties, including extreme hardness,[1] which only diamond and cubic boron nitride exceed, thermoelectricity[2], and a wide semiconducting band gap[3]. It exists in a rhombohedral crystallographic structure with a unit cell comprising an icosahedron and a three-atom linear chain (Figure 1).[1] While the nominal structure has twelve B atoms in the icosahedron and three C atoms in the chain, density functional theory (DFT) calculations of free energy have shown that at least six polytypes of B_4C, which differ in the B and C compositions of the icosahedral and chain structural units, are within 0.2 eV/atom.[4] Three of these polytypes, $B_{11}C^p$-CBC (where the superscript p indicates that the C is in an icosahedral polar position, shown in Figures 1 and 2), B_{12}-CCC, and B_{12}-CBC, are known to constitute a major portion of any boron carbide sample produced by conventional synthesis with $B_{11}C^p$-CBC known to constitute as much as up to 90% by weight.[1,4,5,6]
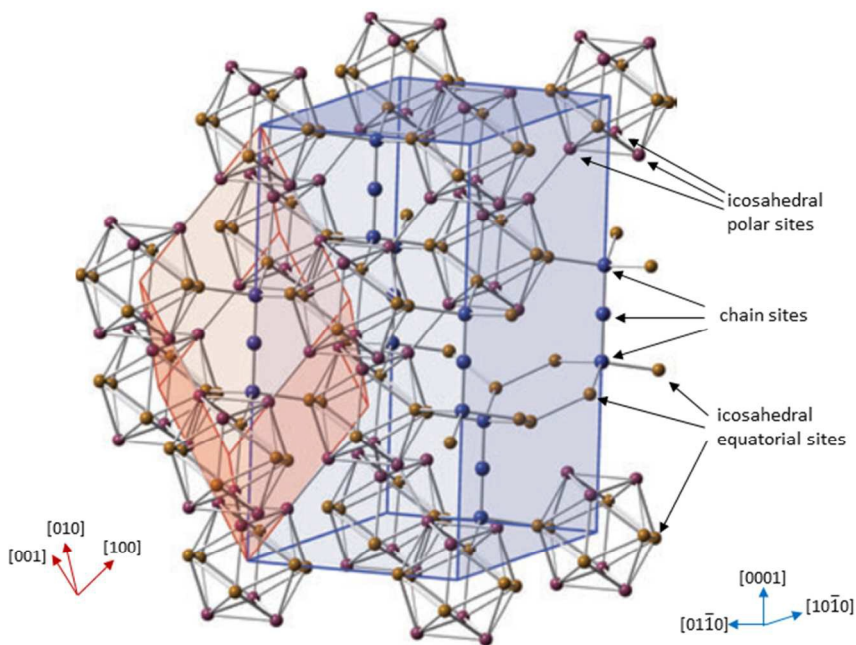
Figure 1. Boron carbide lattice showing relation between the rhombohedral (red) and the hexagonal (blue) unit cells. Inequivalent lattice sites are marked by arrows (Reproduced with permission from The Journal of American Ceramic Society, Wiley Publications).

Some of the mechanical properties of B_4C, for example its high compression strength[7] of 3900 MPa, high Hugoniot elastic limit[8] (maximum stress supported under one-dimensional shock deformation) of 18-20 GPa, and low density[9] of 2.52 g/cm^3, are very attractive for structural applications. However, once the yield stress is exceeded, B_4C softens, rather than hardening like other practical structural materials such as SiC, greatly reducing the amount of energy it can dissipate and therefore limiting its technological usefulness.[10-14] The reason for this poor strength above the elastic limit has been attributed to glass-like behavior[11] and phase transformations[12]. However, other studies have contradicted this explanation,[13] and shown that plasticity in B_4C is accompanied by formation of amorphous bands leading to strain localization and softening.[14-17] Atomistic simulations have attributed the formation of these amorphous bands to the bending of the three-atom chains and crosslinking or breakup of the icosahedra.[18-19] While there is still no coherent view of the atomistic details of the failure mechanisms consistent with all simulation and experimental evidence, it is clear that the details of chemical bonding in B_4C will strongly affect its properties. The insertion of various elements into the lattice could therefore have strong effects on its behavior. For example, elemental alterations at the three-atom chain are likely to impact events such as chain bending, crosslinking of the chain to the icosahedra and the amorphization of the chains, especially with regard to the conversion of the C-C-C chain variety to amorphous carbon. Electronic and vibrational properties that control semiconducting behavior and thermoelectricity will also be affected by changes in valence, bond strength, and atomic mass due to elemental substitutions. Thus, these B_4C-derived materials could be useful for a host of applications such as ballistics systems, pulse detonation systems, and high temperature electronics, including advanced thermoelectric materials.

In this study, we present DFT calculations of the energies of seven substitutional elements (Be, N, Mg, Al, Si, P, and S), and compare their tendency to become incorporated in different sites of the icosahedron-chain structure for the three polytypes mentioned above: B_{12}-CCC, B_{12}-CBC, and $B_{11}C^p$-CBC. As a first experimental test of elemental inclusion into the B_4C lattice, we used the simple, top-down technique of high-energy ball-milling (HEBM) to alloy it with Si, and analyzed the resulting

material by X-ray diffraction (XRD), high-resolution transmission electron microscopy (HRTEM), Raman, [11]B, ^{13}C and [29]Si magic-angle spinning nuclear magnetic resonance (MAS NMR), electron spin resonance (ESR) and X-ray photoelectron (XPS) spectroscopies to elucidate the position of the Si inclusion in the B_4C lattice.

Experimental Section

Materials and instrumentation. B_4C powder was used as-received from Electro Abrasives, Buffalo, NY. The elemental inclusion of silicon was performed by the HEBM of B_4C (3 g, 0.018 mol) and silicon (0.165 g, 0.006 mol; in the form of a chip) using stainless steel media. We note that at this ratio enough Si is present to effect a single substitution event in up to 33% of the unit cells present in the B_4C sample. The HEBM was performed in three sessions of 90 min each with a break of 5 min between the sessions using a reactants-to-media ratio of 1:10. The ball-milled, silicon-substituted B_4C product (B_4C:Si) was subsequently characterized by XRD, HRTEM, Raman, solid-state ^{11}B, ^{13}C and ^{29}Si MAS NMR, ESR and XPS spectroscopic analyses.

DFT calculations. We simulated the relaxed structure of B_4C with various elemental substitutions using the libAtoms/QUIP[20] *eval* program with energies, forces, and virials from the VASP[21,22] DFT program. For VASP, the Perdew-Burke-Enzerhoff exchange-correlation functional[23,24] was used with the standard VASP projector augmented wave (PAW) files[25,26] for B, C, Al, Be, Mg, N, P, S, and Si, with 3, 4, 3, 2, 2, 5, 5, 6, and 4 electrons in valence, respectively. All calculations used a cutoff of 500 eV with VASP precision set to "accurate", electronic Gaussian smearing with a temperature of 0.05 eV, no symmetry, and Γ-centered 4×4×4 Brillouin-zone sampling. Self-consistency was iterated with an energy tolerance of 1×10^{-6} eV. Configurations were relaxed with the conjugate gradient algorithm implemented in libAtoms/QUIP (*eval* program option "cg_n") with a convergence tolerance of 0.001 $eV^2/Å^2$ on the squared norm of the gradient vector composed of atomic forces and virial per atom x $Å^{-1}$.

  For the initial structures of substitutions at various sites in the B_4C lattice, we started with the 15-atom primitive cell consisting of a B_{12} icosahedron and a C_3 chain, and created the two variants, B_{12}-CBC and

$B_{11}C^p$-CBC, by changing the atomic species appropriately. We then substituted the various impurity

elements on all inequivalent sites, which can be divided into four types: chain center, chain end,
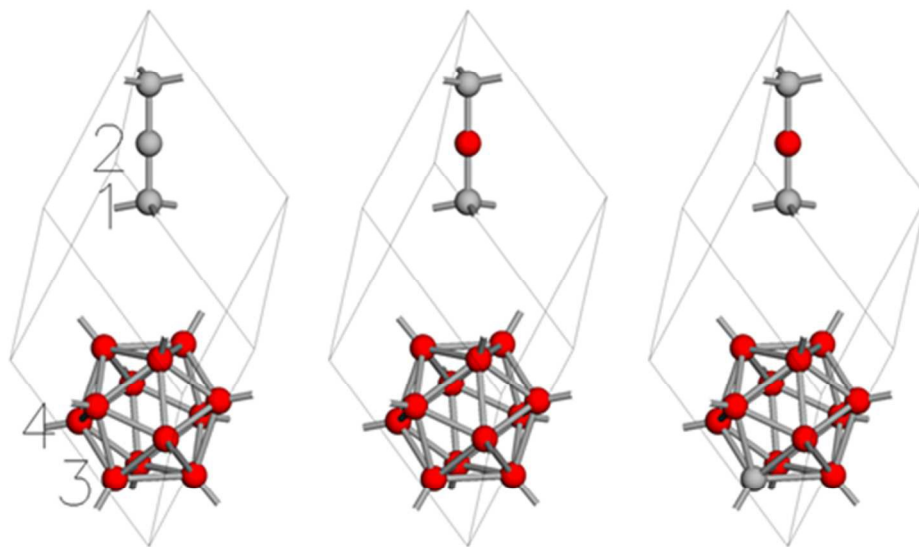
Figure 2: Visualization of the B_{12}-CCC, B_{12}-CBC, and $B_{11}C^p$-CBC primitive cells (left, center, and right panels, respectively), with B represented by red spheres and C represented by grey spheres. Labels on B_{12}-CCC structure show (1) the chain end, (2) chain center, (3) icosahedral polar, and (4) icosahedral equatorial substitutional sites.

icosahedron polar and icosahedron equatorial (Figure 2). The chain center site is bonded to the two

other chain atoms, while the chain end site is bonded to the chain center site and to three icosahedral

equatorial sites. The icosahedral polar sites are bonded to five sites in the same icosahedron and one

site in a different icosahedron, and the equatorial sites are bonded to the chain end and to five other sites

in the same icosahedron. Each configuration was relaxed by perturbing all atomic positions (to break

the symmetry) and minimizing its energy with respect to atomic positions and unit cell size and shape.

Because the net energy difference for each substitution depends on the chemical potentials of each of

the elements involved, we also calculated reference total energies of C and B in the diamond structure

and 105-atom β structure, respectively, relaxed using DFT with respect to atomic positions and unit cell

size and shape. With these reference energies we calculated the relative formation energies of the

substitutions between compositions with varying numbers of B and C atoms, allowing us to energetically order the different sites for each element. Note that comparing the formation energy of different elemental substitutions to each other would also require chemical potentials for the substituting elements, which we have not calculated.

Materials Characterization. We collected HRTEM images of the Si-substituted B_4C on a JEOL 2200 analytical transmission electron microscope operating at 200 KeV. To determine the distribution of B, C and Si, fine probe energy dispersive X-ray spectroscopy (EDS) was employed with a probe size of 1 nm in the scanning TEM (STEM) mode. XRD analyses were performed using a Rigaku 18 kW x-ray generator and a high-resolution powder diffractometer. XRD scans were obtained using Cu $K\alpha_1$ radiation from a rotating anode x-ray source. The crystallite size was determined using the Halder-Wagner method and analysis of the observed peaks after correcting for instrumental broadening, using an external Si standard, at their full width at half maximums (FWHMs).[27] Elemental composition and chemical state analyses were performed using a K-alpha (Thermo Scientific) spectrometer equipped with a monochromated Al $K\alpha$ X-ray source, the energy of which was regularly calibrated and maintained at 1486.6 ± 0.2 eV. The binding energy (BE) scale of the spectrometer was regularly calibrated using an automated procedure to produce Au $4f_{7/2}$, Cu $2p_{3/2}$, and Ag $3d_{5/2}$ peaks within <0.05 eV of standard reference BE values.[28] The microfocused X-ray source illuminated a spot of ca. 400 × 600 μm^2; spectra were collected at three spots for both B_4C and the B_4C:Si samples. Survey spectra were acquired with a 1 eV step size at a pass energy (PE) of 200 eV and high-resolution spectra with a 0.05 eV step size at a PE of 20 eV. XPS spectra were fitted in Unifit (ver. 2011), using a combination of Lorentzian and Gaussian line shapes to fit individual components, and backgrounds were modeled using a combination of Shirley and linear functions. Elemental compositions were quantified using calibrated analyzer transmission functions, Scofield sensitivity factors[29] and effective attenuation lengths (EALs) for photoelectrons; EALs were calculated using the standard TPP-2M formalism.[30,31] Raman spectra were collected on an inVia Raman Microscope (Renishaw) using the 514 nm line of a multi-line argon ion laser as the excitation source. Scans were obtained at ca. 15 mW laser power at the sample and an

integration period of 30 s, with five scans being accumulated. Solid state NMR spectra were obtained in an Agilent 500 MHz spectrometer with a 3.2 mm magic-angle-spinning probe, spinning in the range of 12–20 kHz. Spectra were recorded at ambient temperature. Carbon-13 spectra were obtained with a single small flip angle pulse, and were externally referenced to tetramethylsilane (TMS) using adamantine as a secondary shift reference. Boron-11 spectra were obtained with the quadrupole echo sequence synchronized to the spin rate. Silicon-29 NMR spectra were externally referenced to TMS using a ground silicon wafer as a secondary shift reference. The as-received B_4C and B_4C:Si powder samples were also characterized by electron spin resonance (ESR) measurements at 9.5 GHz in a commercial (E-300) Bruker 9.5 GHz spectrometer. The samples were washed with a diluted HCl solution to remove any residual Fe or other metallic impurities introduced during the manufacture of the native sample and/or during the ball-milling process with stainless steel media. The spectrometer was equipped with a liquid helium flow system that allowed for temperature control from 4.2 – 300K. Typical microwave powers of 5 mW with 2 G modulation amplitude and 100 kHz field modulation were employed for these experiments.

Results and Discussion

DFT. The relative energies of each element in the four types of lattice positions (chain center and end, and icosahedron equatorial and polar) are listed in Table I. For the two structures with B_{12} icosahedra and symmetric chains every site of a given type is equivalent, but forming $B_{11}C$ icosahedra breaks the symmetry, and for that structure we list the lowest energy of each type. For B_{12}-CCC, all substituted elements had a lower energy when replacing C at chain sites compared to B at icosahedral sites. The metallic elements (Be, Mg, Al, Si) had lower energies at the chain center position, while N and S had lower energies at the chain end position, and P was nearly degenerate in energy between the two chain sites. While the general pattern remains, substituting B for the chain center site changed this ordering somewhat for Si: the chain center and polar sites were close in energy for Si (polar is lower by 0.3 eV in B_{12}-CBC), while N, P and S were lowest in energy at the chain end site. The more striking results were obtained for the structure with the $B_{11}C^p$ icosahedra, which as mentioned is the most abundant

component in any commercial sample of B_4C. The metals, Be, Mg and Al, and the non-metals, N and S, were seen to prefer the chain center position and the chain end position, respectively, as with B_{12}-CCC and B_{12}-CBC. However, both Si and P preferred the polar position over any other position. In fact, for Si the next favored position of chain center has a relative energy of 2.3 eV. This interesting general bifurcation of the preference of metals for the chain center and of non-metals for the chain ends, in hindsight, follows chemical preferences of these atoms as metallic elements such as Be, Mg and Al will avoid the chain ends which demand covalent interactions and non-metals such as N and S and to a large extent P will prefer the chain ends as they prefer to covalently bond. However, intuitively predicting such preferences becomes tricky for the semimetal Si as it can have almost equal preferences for all sites in terms of bonding except for size restrictions. Thus, it is interesting to find that Si prefers the polar sites the most. (The structure of the lowest energy configuration of Si substitution in $B_{11}C^p$-CBC is given in supplementary information (SI) Figure S1). This preference by Si may strictly be based on thermodynamics, as substituting the polar position will result in minimal perturbation and in the retention of the overall structure with optimal expansion (SI: Table S1); the corresponding VASP POSCAR files are given in Table S2 (SI). Similar lattice constants and cell volumes for other elements are given in Table S3 (SI). In contrast, when Si substitutes the chain center in $B_{11}C^p$–CBC it results in extra electrons occupying the conduction band affecting the energy of the resulting structure. Due to its unique inclination, we chose Si as an interesting candidate in the first step to experimentally test the feasibility of these predictions. Towards this, we computed the energy for forming a Si-substituted structure among all the three B_4C polytypes, B_{12}-CCC, B_{12}-CBC, and $B_{11}C^p$-CBC commonly found in a typical B_4C sample, in all the various lattice sites relative to lowest energy site over all structures (SI: Table S4). A list of the substitutional energies of all the $B_{11}C^p$-CBC sites are given in Table S5 (SI). Interestingly, while the chain center was the lowest energy site for B_{12}-CCC, for B_{12}-CBC and $B_{11}C^p$ - CBC it turned out to be the polar sites. Given a mixture of these three polytypes, the first four substitutional events that a Si atom would undergo is as follows:

B_{12}-CBC (Polar: 0 eV) = $B_{11}C^p$ -CBC (Polar: 0 eV) < B_{12}-CCC (Chain center: 0.35 eV) = B_{12}-CBC (Chain center: 0.35 eV).

We find that Si substitution increases the volume of the unit cell in all cases, but the magnitude of the change and the proportion of increase along each crystallographic direction varies by site and polytype. In general, substitution on the chain center site leads to the smallest increase in volume, and the chain end site the largest.

Table I. Relative energy (eV) for forming structure with substituting element in different B_4C lattice sites. All energies are relative to the lowest energy site for a given structure and element. For $B_{11}C^p$-CBC, where inequivalent sites of each type exist, the lowest energy site of each type is listed.

Structure	Element	Chain Center	Chain End	Equatorial	Polar
B_{12}-CCC	Be	0.0	6.2	3.0	3.7
	N	0.44	0.0	1.7	1.8
	Mg	0.0	3.6	3.5	3.7
	Al	0.0	4.1	2.9	2.9
	Si	0.0	2.4	2.9	2.0
	P	0.0	0.06	1.9	0.6
	S	1.5	0.0	3.7	2.8
B_{12}-CBC	Be	0.0	1.6	2.7	2.8
	N	4.1	0.0	4.4	3.7
	Mg	0.0	1.4	2.7	2.6
	Al	0.0	0.9	2.3	1.8
	Si	0.3	3.3	0.6	0.0

	P	1.4	0.0	1.6	0.7
	S	1.2	0.0	2.3	1.7
$B_{11}C^P$-CBC	Be	0.0	0.9	1.5	1.5
	N	2.1	0.0	1.9	1.4
	Mg	0.0	0.6	2.1	1.0
	Al	0.0	1.9	1.1	0.3
	Si	2.3	3.6	2.9	0.0
	P	2.2	1.3	1.6	0.0
	S	0.9	0.0	1.4	0.3

HEBM: To experimentally test the DFT predictions of preferences for elemental substitution, in this case for that of Si, we realized that previous attempts involved mainly sintering techniques that required temperatures of greater than 1500 ^{o}C.[32] It is well known that the crystal lattice of B_4C becomes unstable above a temperature of 1100 ^{o}C as carbon atoms start to diffuse from its lattice above this temperature.[33] In the previous attempts it is likely that in the Si-substituted products the original crystal lattice of B_4C would not have been retained, thus producing phase separated structures including ones containing SiC. In contrast, the HEBM process offers a technique by which elements can be substituted into the existing crystal lattice at much lower temperatures (~200-400 ^{o}C).[34] Such a low temperature pathway can provide a means to effect the substitution of Si in B_4C without detrimentally altering the starting crystal structure. Since HEBM is a non-equilibrium process, it can produce lattice defects enabling and enhancing the diffusion of the solute (Si in this case) in the solid state into the B_4C atomic lattice. Also, because B_4C is an extremely hard material, it is likely that such defects (such as dislocations, vacancies, stacking faults and grain boundaries) in themselves will not significantly alter the lattice structure.

From a fundamental sense, it would also be interesting to study the nature, order of production and extent of such lattice defects; however, it is beyond the scope of this paper.

XRD. The diffraction scans of as-received B_4C and B_4C:Si are shown in Figure 3. All peaks were indexed based on the rhombohedral lattice R-3m(166) of B_4C. The starting material lattice parameters were
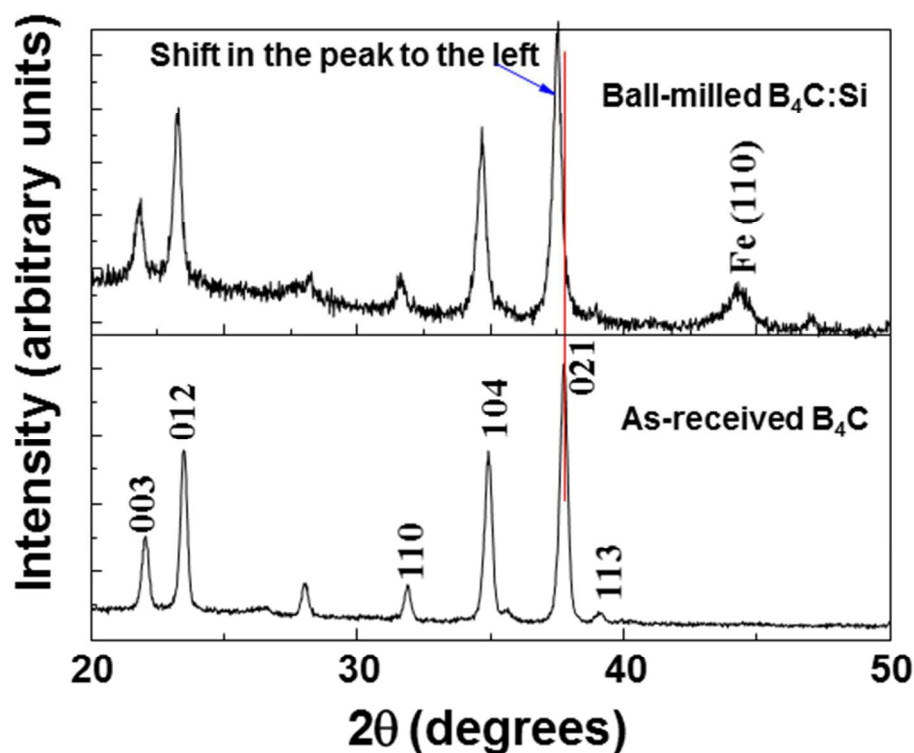
Figure 3. $2\theta/\theta$ scans of ball-milled B_4C:Si and as–received B_4C powders collected with Cu Kα_1 radiation. The unassigned peak in the as-received B_4C belongs to the commonly found B_2O_3 contaminant.

determined to be a = 5.608 Å and c = 12.07 Å, by using the least squares refinement of the observed reflections, in reasonable agreement with the reported bulk lattice parameters of a = 5.61 Å and c = 12.14 Å for the rhombohedral phase of B_4C (PDF#01-075-0424).[35] In fact, the lattice parameters of a = 5.608 Å and c = 12.07 Å of the as-received B_4C lie very close to DFT calculated values of the $B_{11}C^P$-CBC polytype (a = 5.60 Å and c = 12.06 Å (Table S1)). In comparison the a and c axes values of the B_{12}-CCC and B_{12}-CBC polytypes are in the range 5.64-5.66 Å and 12.12-12.13 Å, respectively, which

suggests that the as-received B_4C contains the $B_{11}C^P$-CBC polytype as the major component, possibly up to 90% by weight as previously reported. This is also further supported by the Raman and NMR analyses of the as-received B_4C (*vide infra*). After Si-substitution B_4C retained its rhombohedral lattice structure indicating that such an incorporation did not drastically alter the original crystal structure. The crystallite size was seen to reduce from 314(16) Å for B_4C to 242(11) Å for B_4C:Si. More importantly, a shift in the peak to lower 2θ was observed which indicates a volume increase of the crystal lattice suggestive of lattice expansion. This allowed for the indexing of all of the peaks of Si-substituted B_4C based on the rhombohedral lattice of B_4C. The lattice parameters of the expanded lattice were found to be a = 5.623 Å and c = 12.14 Å, corresponding to a 1.40% expansion of the rhombohedral lattice's volume on Si substitution. However, the volume change of 1.40% (i.e. equivalent to ~15% substitution of the available B_4C unit cells) suggested that all of the provided Si did not participate in substitutional events as a complete substitution of one-third of the unit cells should have produced a lattice expansion of ~3.4%. The volume expansion value should have significant contributions from the energetically favored Si substitutions at the icosahedral polar sites of the major component $B_{11}C^P$-CBC and the minor component B_{12}-CBC along with minor contributions from the slightly less energetically favored sites of chain centers in B_{12}-CCC and B_{12}-CBC. To determine whether a greater degree of substitution could have resulted had enough Si been provided to substitute all of the B_4C cells in a sample, we performed a similar ball-milling experiment utilizing three times as much Si as before. The lattice expansion value obtained from the XRD analysis of the resulting product showed that even under this condition only ~18% of the unit cells are substituted (SI: Figure S2). Hence, it appears that *under the non-equilibrium processing conditions of HEBM* utilized in this *study* the extent of Si diffusion into B_4C crystallites of ~ 30 nm size is limited and may possibly occur only in about one-fifth of the unit cells in the ball-milled B_4C sample assumed to be localized at the surface of the crystallites. We also considered the possibility that the expansion in the volume of B_4C's lattice on ball-milling with Si was caused just by the process itself and not due to Si substitution. To verify this, we ball-milled the same amount of B_4C, in the absence of Si, under the same conditions and characterized the product by XRD analysis (SI: Figure

S3). There was no shift in the 2θ values of this product when compared to those of B_4C's, thus, excluding the possibility that ball-milling alone causes an expansion in the volume of the B_4C lattice.

  In order to determine the site of Si substitution, we performed detailed Rietveld analysis on the as-received B_4C and ball-milled B_4C:Si samples. The Rietveld analysis of the XRD profile of the as-received B_4C sample yielded lattice parameters of a=5.59737(±0.0004) Å and c=12.07149(±0.000801) Å and atomic coordinates given in Table II with an R factor of 6.22%. On the other hand, Rietveld refinement of the XRD profile of the ball-milled B_4C:Si sample yielded lattice parameters of a=5.60561(±0.004) Å and 12.08961 (±0.00149) Å and atomic coordinates given in Table III with an R factor of 8.9%.

Table II. Atomic coordinates after Rietveld refinement of the XRD profile of the as-received B_4C sample.

ID	Site	Occupancy	x	y	z	Biso
B	18 (Equatorial)	1	0.16169	0.83831	0.64089	1.67
B	18 (Polar)	1	0.22386	0.77613	0.78029	1.53
C	6	1	0	0	0.61874	1.06
B	3	1	0	0	0.5	1.83

Table III. Atomic coordinates after Rietveld refinement of the XRD profile of the B_4C:Si sample.

ID	Site	Occupancy	x	y	z	Biso
B	18 (Equatorial)	1	0.16297	0.83703	0.64143	0.36
B	18 (Polar)	1	0.22579	0.77421	0.78039	0.39
C	6	1	0	0	0.61874	0.63
B	3	1	0	0	0.5	0.38

Substitution of Si on site 18 (polar) for B, site 18 (equatorial) for B, site 6 (chain end) for C and site 3 (chain center) for B with occupancies of 0.03 for Si and 0.97 for the respective elements gave R factors of 7.76%, 8.83%, 7.18% and 7.35%, respectively, suggesting comparable preferences for substitution at the polar, chain end and chain center sites with R values within ~0.5%, however, yielding a higher value for substitution at the equatorial sites (Table S6). We note that the above R values were obtained by refining Si-substituted rhombohedral unit cell of B_4C ($B_{13}C_2$: PDF#04-004-4255)[36] containing only B_{12} units and not the more prevalent $B_{11}C^p$-CBC unit cell with $B_{11}C^p$ units, as refinement with such a structure yielded high R values of >35%. In line with the substitutional efficiency value (~15%) obtained from the lattice cell expansion determination, the occupancy value of 0.03 of Si suggests that only ~18% of the unit cells are substituted by Si even though there was enough Si for substituting in one-third of the unit cells in the ball-milled B_4C sample. While the lower R value for the chain center substitution could be possibly attributed to an energetically favored substitution by Si in the minor components B_{12}-CCC and B_{12}-CBC, the value of 7.18% for chain end substitution is surprising as in none of the three B_4C polytypes is such a substitution suggested to be energetically favored by the DFT results! While one cannot discount the possibility of Si substitution in chainless B_4C unit cells[37] or in chains with vacancies[37] to give such chain end substitutions, the observed a and c axes values exclude such possibilities. For example, the a and c axes values of the likely product $B_{12}Si_2$[38] in a such scenario are 6.330 Å and 12.736 Å, respectively, which are much higher than the values observed for B_4C:Si. In addition, the substitution of Si in possible vacant chain sites would have significantly altered the region around 500 cm^{-1} in the Raman spectrum of B_4C:Si with respect to that of the as-received B_4C which happens to be not the case (*vide infra*). There was also no evidence of a significant amount of vacancies in the ^{11}B and ^{13}C NMR spectra of the as-received B_4C. Importantly, the greater changes in the x and y atomic coordinates for site 18 (polar) in Table III from the Rietveld refinement of the XRD profile of ball-milled B_4C-Si sample supports the substitutional event at the polar sites in $B_{11}C^p$-CBC to be the most probable one. Also, the DFT results indicate that Si substitution of the polar sites in $B_{11}C^p$-

CBC are more favored than such substitutions at the chain end and chain center sites by 3.6 and 2.3 eV, respectively.
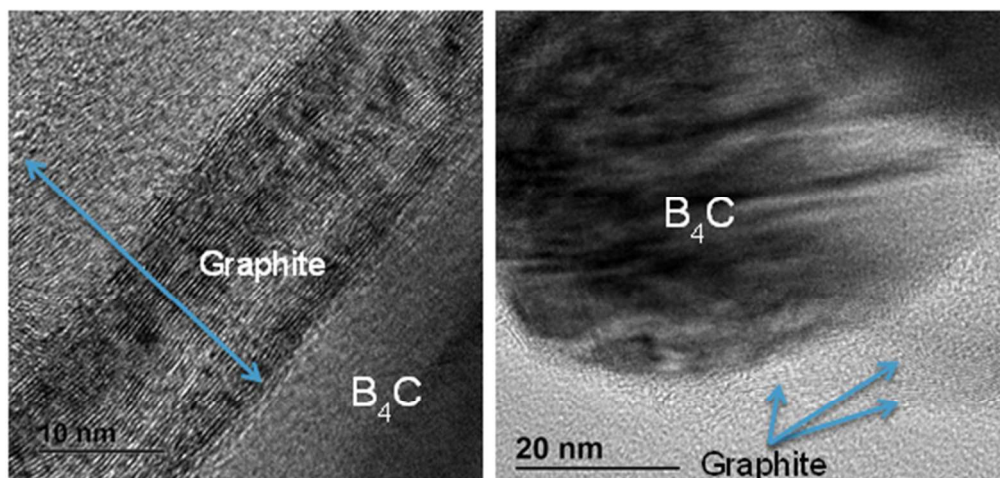
Figure 4. HRTEM of the as-received B_4C sample showing graphitic layers around B_4C grains.
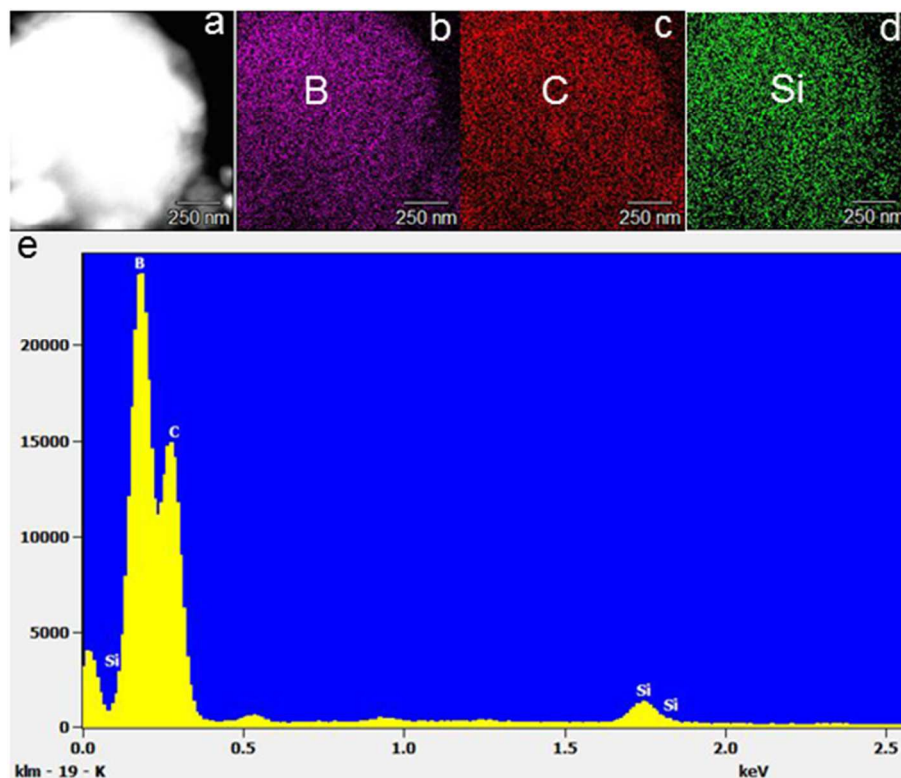
Figure 5. Fine probe EDS scans of a B_4C:Si particle (5a) showing the concentrations of B (5b), C (5c) and Si (5d) in the particle. The EDS spectrum (5e) extracted from the above EDS scan showing the considerable presence of Si in the B_4C lattice.

HRTEM. Figure 4 shows the HRTEM of the as-received B_4C powder which exhibits the presence of graphitic layers on B_4C grains. The high energy collisions of the media during HEBM with the mixture of B_4C and Si components presumably breaks these graphite layers and create lattice defects in B_4C enabling and enhancing the diffusion of the solute (Si) in the solid state into the B_4C atomic lattice.

In order to confirm that Si has entered into B_4C lattice, we studied the distribution of Si and performed HRTEM imaging to investigate any evidence for phase separation on the nano scale and to measure the lattice spacing of B_4C. Figure 5 shows the fine probe EDS maps from a number of powder particles of the B_4C:Si product illustrating the distributions of Si, B and C in the sample. The uniform dispersion of Si in the image (Figure 5d) suggests that the substitution of Si in the sample is uniform and that there is no Si segregation or phase separation. The extracted EDS spectrum, as shown in Figure 5e, demonstrates
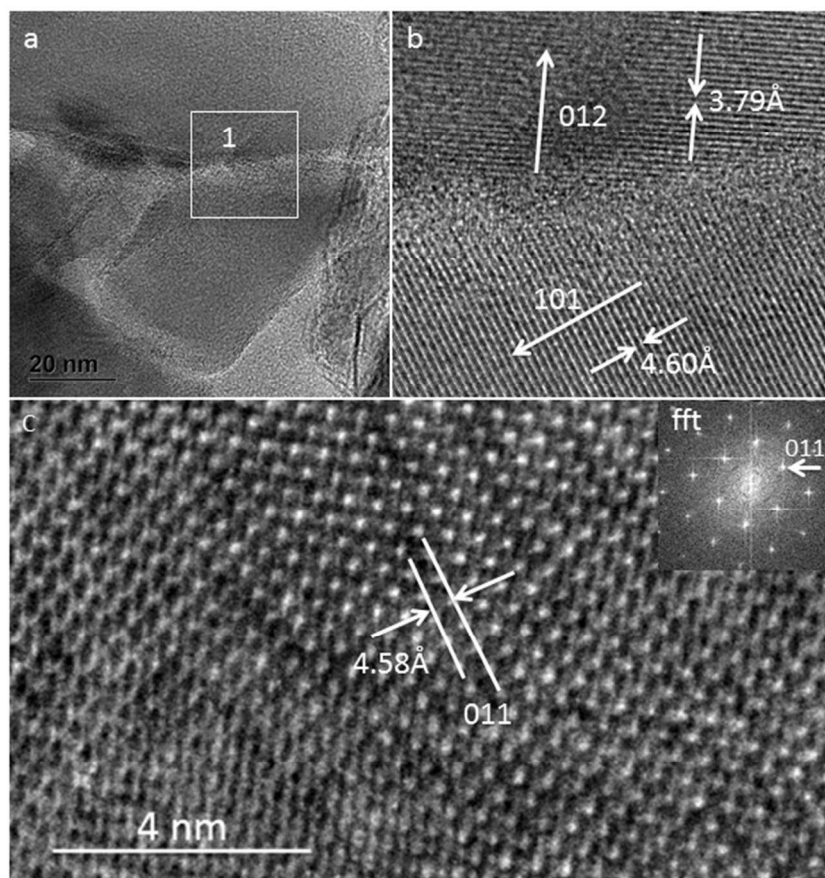
Figure 6. (a) HRTEM of B_4C:Si showing (b) an increase in the lattice of {101} planes including the lattice image of the [2-10] zone (c).

the presence of considerable amount of Si in the B_4C lattice. We have also observed an increase in the lattice spacing as a result of Si incorporation, consistent with the XRD observation. Figure 6a shows the HRTEM image of the B_4C:Si product and Figure 6b, obtained from the box in Figure 6a, and the corresponding lattice image of the [2-10] zone in Figure 6c show a considerable increase in the lattice spacing of the {101} planes. Based on XRD and TEM observations we can conclude that the HEBM of B_4C and Si powders produces a solid solution of Si in B_4C at a relatively low temperature *without detrimentally impacting its lattice structure.*

Raman. The rhombohedral boron carbide structure B_{12}-CBC with D_{3d} symmetry is predicted by group theory to have 12 modes, of A_{1g} (5) and E_g (7) symmetry, that are Raman active.[39] The Raman spectrum obtained at excitation wavelength of 515 nm (2.41 eV) of the as-received B_4C agrees well with a previous report of such measurements (Figure 7).[40] The two narrow bands centered around 500 cm^{-1} have been
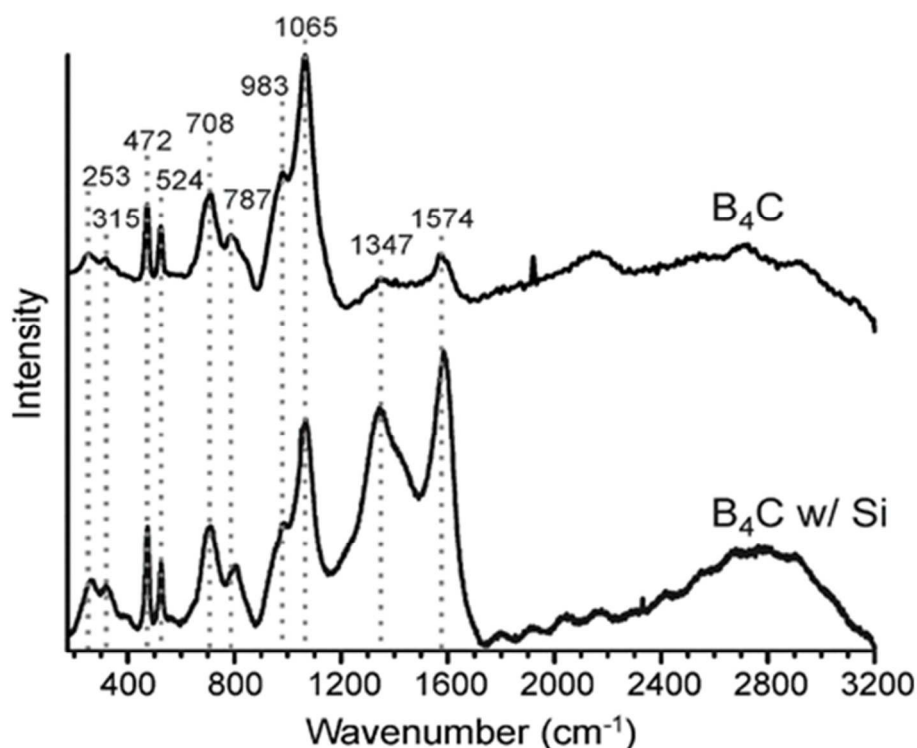
Figure 7. Raman spectra of B_4C and B_4C:Si powders excited by a 514.5 nm Ar ion laser.

assigned to the stretching vibrations in the soft CBC chains found in B_4C composition with $\leq 20\%$ C; thereby supporting the presence of more than 90% of the $B_{11}C^p$-CBC polytype in the as-received B_4C sample.[41] In boron-rich boron carbides such as B_{12}-CBC these peaks were found to be almost non-existent.[41] Furthermore, the Raman spectra of the B_4C and B_4C:Si powders exhibited characteristic peaks for crystalline B_4C (Figure 7).[1] The agreement in the positions and relative intensities of the peaks in the region ranging from 400 to 1200 cm^{-1} indicated that the symmetry of the icosahedra was not altered by the HEBM process. The lack of major changes in the bending vibrations around 500 cm^{-1} of the 3-atom chain resonances in the as-received B_4C and B_4C:Si further rules out the chain end substitution of any of the polytypes as such substitutions are expected to produce major changes in the resonances.[41] However, we observed clear differences in the intensities of the bands below 400 cm^{-1}, which have been attributed to soft phonons associated with B_4C lattice distortion[42]; however, these bands have been shown to vary between samples taken from the same bulk material.[41] Also, while there was significant intensity enhancement in the peaks corresponding to the graphitic (G) and disorder-induced (D) carbon modes centered at 1574 and 1347 cm^{-1}, respectively, in the spectrum of the B_4C:Si powder, the relative intensities of the G and D bands were fairly consistent. Thus, the increase in the intensity of the carbon peaks in the B_4C:Si sample is more likely a result of the unreacted Si atoms having a surface enhancement effect on graphitic contaminants in close proximity,[43] rather than by B_4C amorphization which would have produced a strong D mode and a weak G mode.[44]

NMR: The boron carbide materials have been characterized with multi-nuclear solid state NMR spectroscopy. NMR signals are normally observed in diamagnetic materials. The electronic spins in paramagnetic materials can have a profound effect on the NMR spectra, potentially leading to very large resonance shifts or broadening of the peaks, in extreme cases resulting in NMR spectra being unobservable.

The central transition peak in the ^{11}B NMR spectrum of B_4C (Figure 8) shows a single peak slightly asymmetric on the downfield (high frequency) side. The main peak is due to the boron in the

icosahedral cages.[45] The asymmetry has been ascribed to an unresolved peak due to boron in the center of the chain.[46] The intensity of the central transition peak in $B_4C:Si$ is diminished relative to the neighboring spinning sidebands by approximately 20%. It is possible that the generation of radical species at the Si-substituted B_4C polytypes wherein the substitution occurs at a boron site caused a reduction in the initial [11]B signal and the broadening of the remnant B signal due to coupling with the unpaired delocalized electron.

The ^{13}C NMR spectrum of B_4C (Figure 8) shows two peaks at 3.5 ppm and 83.5 ppm which have been assigned previously to carbon at the chain ends and in the polar position of the icosahedra, respectively, with no detectable chain center carbon signal for the B_{12}-CCC polytype.[46-48] No peak attributable to graphitic carbon is observed; however, such a peak is expected to be broad and possibly below our detection limit. The peak marked with an asterisk comes from the poly(tetrafluroethylene) rotor cap. The carbon spectrum of $B_4C:Si$ shows the same two peaks with the same ratio of intensities, within experimental uncertainty. Quantitative measurement of the peak heights shows that the intensities of the
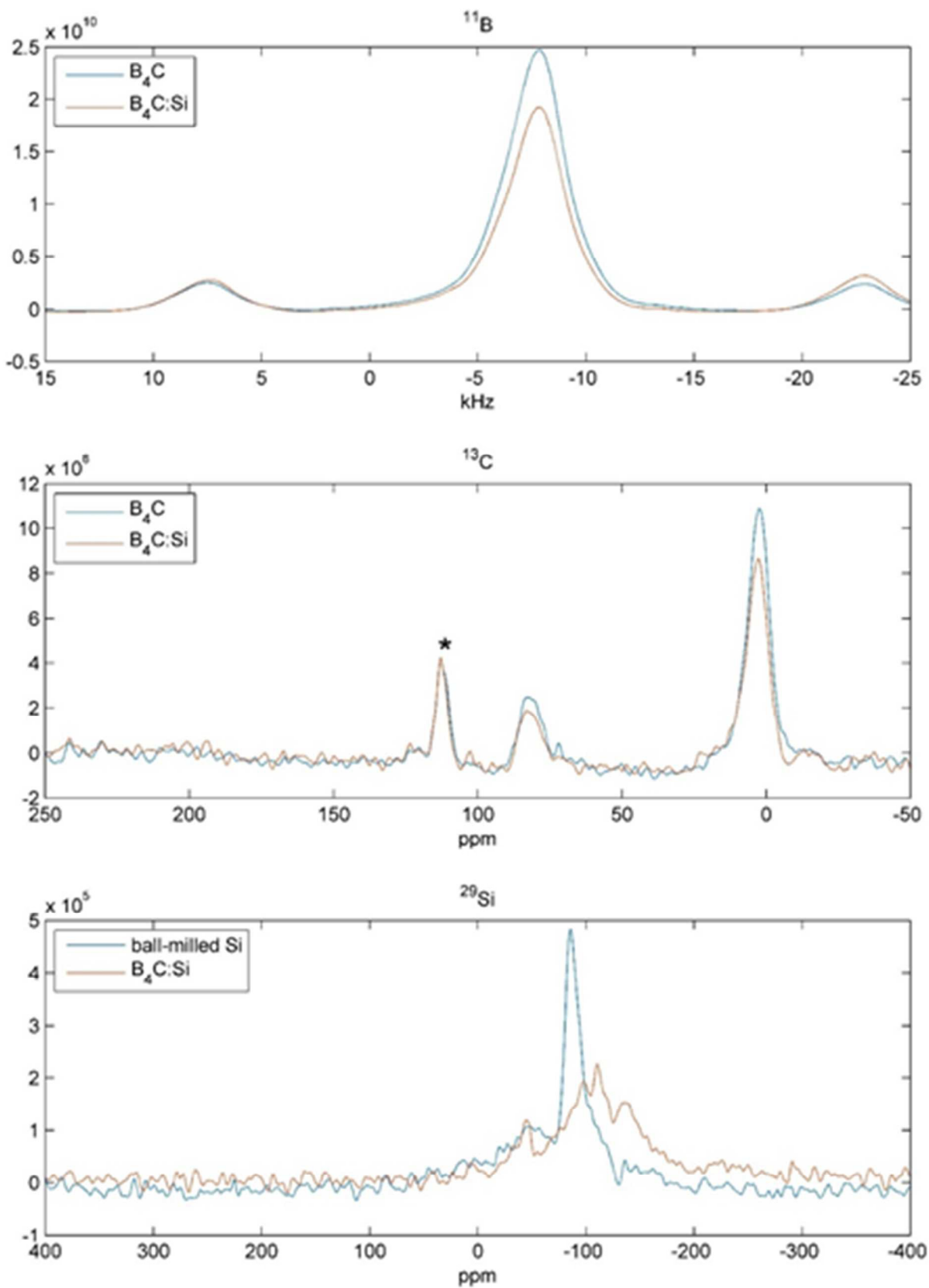
Figure 8. ^{11}B, ^{13}C and ^{29}Si MAS NMR spectra of B_4C and B_4C:Si powders.

carbon peaks in $B_4C:Si$ are reduced by 22 ±3% and 26 ±9% for the chain end and polar position peaks, respectively, similar to the reduction in the boron signal intensity. Wade's electron counting rules of polyhedral boranes[49] and theories on the bonding in B_4C[37] can provide insights into these changes in the intensities of the carbon peaks and the above discussed reduction in the intensities of the boron peaks. It is obvious that the substitution of the chain ends sites by Si in any of the three B_4C polytypes will not produce a reduction in the carbon peak at the polar position. The observed reductions appears more reasonable if one were to consider the substitution of the polar sites by Si in the *major component* $B_{11}C^p$-CBC to which MAS-NMR measurement should be more sensitive. Since among the six polar sites in the $B_{11}C^p$, the substitution by the 'isovalent' Si at the C^p site is found to be more favored than the other five polar boron sites by at least 2.2 eV (Table S5), such a substitution will only reduce the intensity of the polar carbon peak and not of the chain end peaks. However, when Si substitutes one of the five 'non-isovalent' boron polar sites the resulting $B_{10}SiC^p$-CBC product's carbon peaks will be broadened due to interaction with the electron spin thereby reducing the intensities of both the polar and chain end carbon peaks. This explains more reasonably the observed changes in the chain end and polar carbon peak intensities.

A sample of the same silicon wafer used in the $B_4C:Si$ was ball-milled and the ^{29}Si NMR spectrum (Figure 8) obtained as a relative shift standard. The silicon shows a relatively narrow peak with the shift of the maximum intensity defined as -85 ppm superimposed on a broad, asymmetric peak with the shift of the maximum intensity at -48 ppm with reference to TMS peak at 0 ppm; the peak has a spin lattice relaxation time of greater than 40 s. The breadth of the peak is greater than that observed in other powdered Si and is most likely due to defects introduced by ball-milling. In contrast, the ^{29}Si NMR spectrum of $B_4C:Si$ shows a very broad peak with maximum intensity at -110 ppm and a spin lattice relaxation time of approximately 20 s. The shift is similar to that observed in a boron-silicon porous glass[50], but the $B_4C:Si$ peak is much broader.
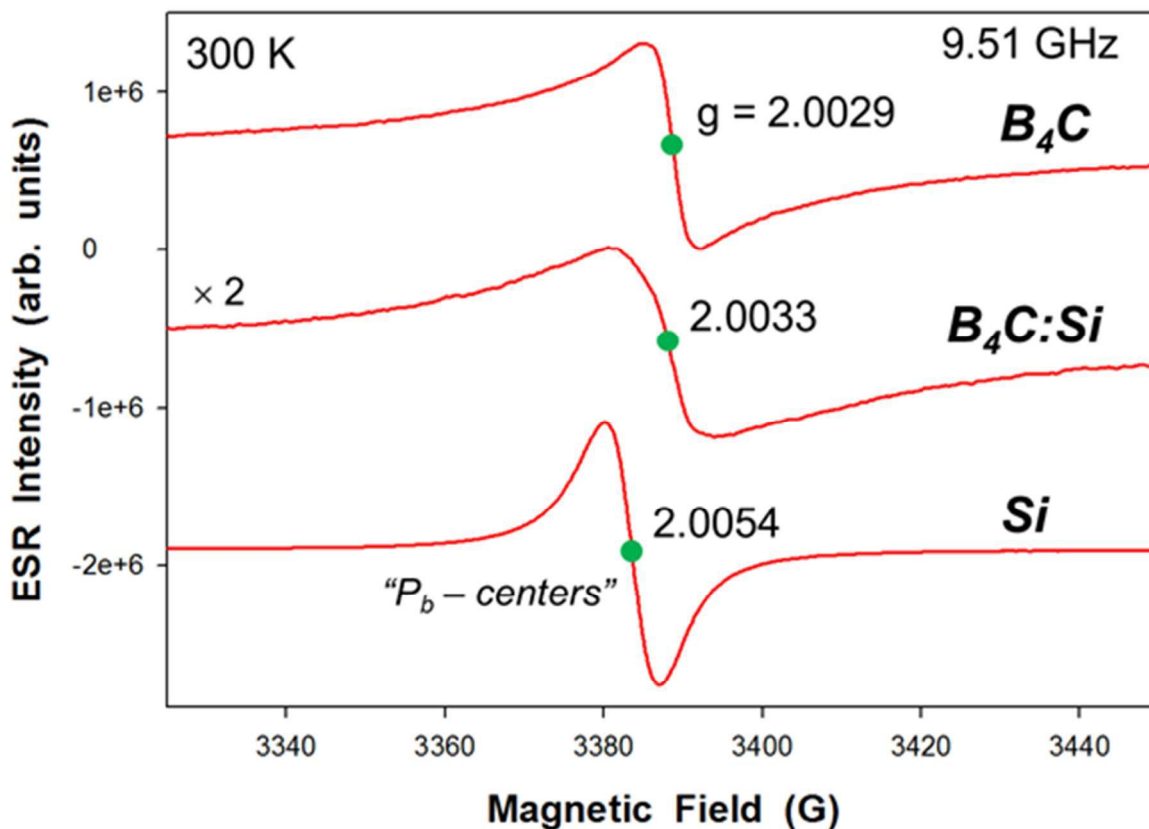
Figure 9. ESR spectra obtained at 300 K for the ball-milled, acid-washed B$_4$C, B$_4$C:Si, and Si powder samples. Note the nearly two-fold increase of the FWHM value for the B$_4$C:Si sample relative to that found for the as-received B$_4$C powder.

ESR: Representative ESR spectra obtained at room temperature for the (ball-milled, acid-washed) as-received B$_4$C and B$_4$C:Si powder samples are shown in Figure 9. In addition, an ESR spectrum was obtained (using the same ball-milling and HCl-washing treatments) for several milligrams of the crystalline Si employed in the preparation of the B$_4$C:Si powder sample. A single, strong ESR signal was observed for the B$_4$C powder with Zeeman splitting g-value of 2.0029 ± 0.0002 and a full-width at half- maximum (FWHM) value of 7.2 G. These magnetic resonance parameters are within error very similar to those reported in the literature for ESR signals observed in boron carbide powders made by various methods as described in Ref. 51. The microscopic origin of this signal has been the subject of much debate over the years, including its association with radical centers[48]. However, its exact origin may not be too critical for this work in understanding what occurs when Si is "energetically" introduced

into the host B_4C powder through the ball-milling process. In particular, as shown in the middle spectrum of Figure 9, a strong ESR signal is also observed for the B_4C:Si powder sample with g-value of 2.0033 ± 0.0004 and FWHM of 13.4 G. This g-value is quite similar to that found for the B_4C powder but its linewidth is nearly double. Following the discussion and analyses presented by Kakazey et al.[52], this increase in linewidth can be understood simply as due to an exchange interaction between the "native" paramagnetic defects (presumably radical centers) in the B_4C lattice and the additional mobile charge carriers at 300K that are generated from replacement of some fraction of the B host lattice atoms with Si shallow donors. We note that the ESR signal observed from ball-milling the crystalline Si alone (see bottom spectrum in Figure 9) is characterized by a g-value of 2.0054 ± 0.0002 and FWHM of 6.9 G. This resonance is a well-known "fingerprint" of so-called P_b-centers and are associated with Si dangling bond defects as also reported recently for ball-milled Si nanoparticles[53] and is consistent with the relatively short spin-lattice relaxation time observed in the ^{29}Si NMR of the ball-milled Si material. Most notably, ESR simulations revealed that one cannot account for the g-value and lineshape (and the broadening, in particular) observed for the B_4C:Si powder sample from the addition of the individual spectra found for the as-received B_4C powder and crystalline Si samples. However, it is possible that the slight inflection observed in the lineshape just below the resonance field position for the B_4C:Si sample may be due to some small contribution from un-reacted B_4C. Overall, these ESR results support our proposal for the incorporation of Si within the B_4C host lattice sites through the HEBM treatment.

XPS. XPS spectra of B_4C and B_4C:Si are shown in Figure 10; elemental compositions are shown in Table S7 (SI). In the B1s region of B_4C, peaks are seen with binding energies that match[54] B-B, B-C and B-O bonds at percentages of 62, 20 and 18, respectively. The B-B and B-C bonds can be attributed to the interactions between the boron atoms in the icosahedron and between boron and carbon within the icosahedron and in the three-atom chain, respectively. The appearance of the B-O binding energy[55] feature indicates the presence of B_2O_3 in the as-received B_4C sample as also seen in its XRD spectrum (Figure 3). In the C1s region of the spectrum, a majority (~90%) of the absorption peaks are seen to
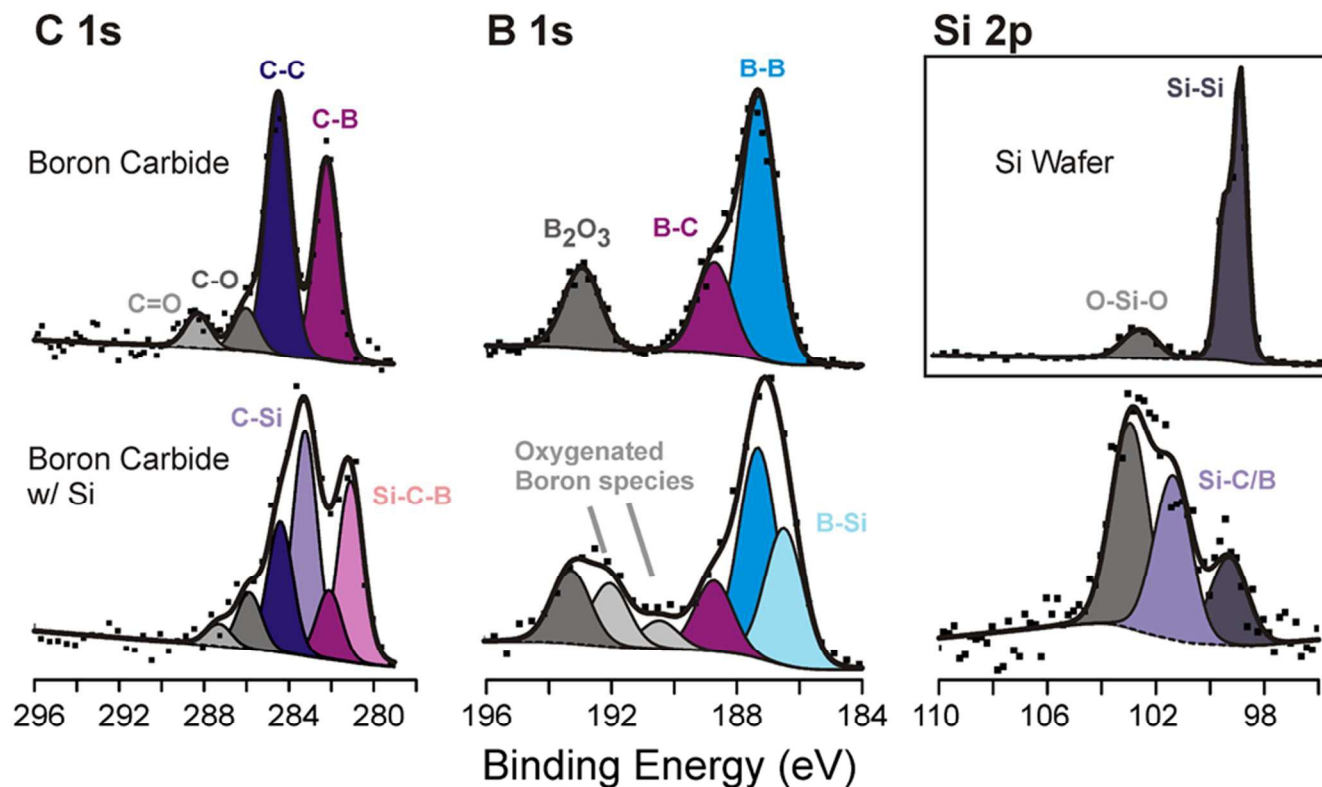
Figure 10. Characteristic high resolution XPS spectra of the C 1s, B 1s, and Si 2p regions of a commercial B_4C sample (top left and top middle), a silicon wafer (top right), and our high-energy ball milled sample with infused Si (bottom).

be associated with C-C and C-B bonding energies, suggesting the presence of interactions between carbon and boron within the icosahedron and the three-atom chain and also among such carbon and boron within them. The large extent of the C-C bonding suggests the presence of free carbon such as graphitic inclusions in the material which are known to be present in typical B_4C samples[56], and as corroborated by HRTEM analysis. The minor components corresponding to C-O and C=O bonds varied between sample collections of both the B_4C and B_4C:Si powders. We attribute the oxygen-containing carbon species to contaminants in the as-received B_4C powder or atmospheric adsorbates typically seen in XPS analysis.

In B_4C:Si, the relative ratio of the B-B to B-C peaks was 2.91 for B_4C and 2.74 for B_4C:Si, respectively, suggesting a greater degree of Si substitution around B-C centers and two minor peaks evolved that we attribute to oxygenated boron species (BE=190-193 eV). More importantly, we

observed a peak at BE=186.5 eV corresponding to B-Si interactions.[55] This peak can be attributed to the Si-B interactions originating mostly from the replacement of one of the polar boron sites in $B_{11}C^p$-CBC and to a minor extent from the replacement of polar boron sites in B_{12}-CBC. In the B_4C:Si XPS spectrum, a peak is also observed at BE=283.3 eV which is typically attributed to bonding interactions between carbon and silicon. This can be attributed to the neighboring Si-C interactions at the polar sites in $B_{10}SiC^p$-CBC and $B_{11}Si$-CBC derived from the substitutional reactions of Si with $B_{11}C^p$-CBC and B_{12}-CBC. Furthermore, the peak at 281.1 eV indicates the presence of a species such as Si-C-B in B_4C:Si, which can arise from the discussed polar substitutions. In the Si 2p region, a peak around 101.1 eV can be attributed to Si-C bond and the peaks at 98.9 eV and 102.6 eV can belong to Si-Si (arising from Si-Si present in unreacted moieties of Si) and O-Si-O (possibly formed from some oxidation of Si) bonds, respectively.

Conclusions

Our DFT simulations predict that, in general, the metallic and semi-metallic elements Be, Mg, Al, and Si preferentially substitute at the centers of the three-atom chains, while the non-metallic elements N, P, and S preferentially substitute at the ends of the chains in B_{12}-CBC and B_{12}-CCC polytypes. However, in the case of the more dominant polytype $B_{11}C^p$-CBC, interesting substitutional preferences were observed especially for Si as it displayed a preference for the polar sites in this B_4C polytype. As an initial test of the DFT predictions, we alloyed B_4C with Si by HEBM, a process that gives us the ability to effect substitutional events in B_4C without detrimentally impacting its crystal structure, and analyzed the bonding and structure of the resulting material by a combination of techniques including HRTEM, XRD, XPS, Raman, MAS NMR and ESR spectroscopies. Our experimental results broadly confirm the general DFT predicted preference for Si to occupy polar sites in the major B_4C polytype, $B_{11}C^p$-CBC. Our work shows the general ability of DFT to predict the structure of chemically interesting substitutions in ceramics, and the power of the simple, top-down technique of HEBM to produce alloys of materials with stiff, mechanically strong and thermally stable lattices, making it possible to modify their properties. In fact, preliminary evaluations, not reported here, have shown that the hardness of

B_4C:Si is nearly double that of the as-received B_4C. While our initial motivation is based on the mechanical properties of B_4C, where the substitutions' effects on bond stiffness and geometry may have dramatic effects, we note that elemental lattice substitution will also affect the electronic, vibrational, and transport properties (both electronic and thermal) of B_4C. Thus, the development of ceramics containing elemental substitutions could lead to a new class of materials whose properties can be tailored for a wide range of applications. In future work it would be interesting to test whether the site preference predictions of our DFT calculations for other elements are also confirmed experimentally, and how the elemental substitutions, with their different valence and bonding tendencies, affect the mechanical, electronic, and vibrational properties of boron carbide.

ACKNOWLEDGMENTS

Electronic supplementary information (ESI) available: Figure S1 depicts the structure of the lowest energy configuration of Si in $B_{11}C^p$-CBC, Figure S2 shows the XRD spectra of the as-received B_4C after MeOH:HCl (95:5) washing and of the B_4C:Si wherein the initial Si:B_4C unit cell ratio is 1:1, and Figure S3 shows the XRD spectrum of the as-received B_4C sample after ball-milling under the same conditions as used during the production of the B_4C:Si sample. Table S1 provides the relaxed lattice constants **a** in [0001] plane (in Å) and **c** along (0001) direction (in Å), and unit cell volume V (in Å^3), Table S2 provides the VASP POSCAR files for B, C and Si in the products formed by substitution of Si in the three B_4C polytypes, Table S3 lists the effects of Be, N, Mg, Al, P or S substitution on lattice

parameters of the three B_4C polytypes, Table S4 gives the energy (eV) for substituting Si in different B_4C lattice sites relative to the lowest energy site over all structures, Table S5 provides the energies of Si substituted at the fifteen unique sites in $B_{11}C^p$-CBC, Table S6 shows the preferences for Si substitutions at site 18 (polar), site 18 (equatorial), site 6 (chain end) and site 3 (chain center) with occupancies of 0.03 for Si and 0.97 for the respective elements with the associated R values and Table S7 provides the elemental compositions of B_4C and B_4C:Si.

REFERENCES

1. V. Domnich, S. Reynaud, R. A. Haber and M. Chhowalla, *J. Am. Cer. Soc.,* 2011, **94**(11), 3605-3628.

2. K-F. Cai, C-W. Nan and X-M. Min, *Mater. Sci. Eng. B: Solid-State Mater. Adv. Techn.,* 1999, **B67**(3), 102-107; J. Li, T. Goto and T. Hirai, *Mater. Trans., JIM,* 1999, **40**(4), 314-319.

3. B. B. Sylvester, S-H. Lin and B. J. Feldman, *Solid State Comm.,* 1995, **93**(12), 969-971; B. W. Montag, K. A. Nelson, N. P. Platt, N. M. Boag and J. I. Brand, *ECS Transactions* 2006, **3**(5), 429-435; N. Hong, M. A. Langel, J. Liu, O. Kizilkaya and S. Adenwalla, *J. Appl. Phys.,* 2010, **107**(2), 024513/1-7.

4. G. Fanchini, J. W. McCauley and M. Chhowalla, *Phys. Rev. Lett.,* 2006, **97**, 035502/1-40.

5. F. Mauri, N. Vast and C. J. Pickard, *Phys. Rev. Lett.,* 2001, **87**(8), 085506/1-6.

6. T. V. Hynes and M. N. Alexander, *J. Phys. Chem.,* 1971, **54**, 5296-5310.

7. Z. Rosenberg, *AIP Conference Proceedings,* 1996, **370**, 543-546.

8. W. H. Gust and E. B. Royce, *J. Appl. Phys.,* 1971, **42**, 276-295; F. Thevenot, *J. Eur. Ceram. Soc.,* 1990, **6**, 205-225.

9. D. Emin, *Phys. Rev. B,* 1988, **38**(9), 6041-6055.

10. D. E. Grady, *J. De Physique IV,* 1994, **4**, C8/385-391.

11. N. K. Bourne, *Proc. R. Soc. Lond. A,* 2002, **458**, 1999-2006.

12. D. E. Grady, *Mech. Mater.,* 1998, **29**, 181; D. P. Dandekar, *U.S. Army Report No. ARL-TR 2456,* 2001.

13. T. J. Vogler, W. D. Reinhart, and L. C. Chhabildas, *J. Appl. Phys.,* 2004, **95**, 4173-4183.

14. M. Chen, J. W. McCauley and K. J. Hemker, *Science*, 2003, **299**, 1563-1566.

15. D. Ge, V. Domnich, T. Juliano, E. A. Stach and Y. Gogotsi, *Acta Mater.* 2004, **52**, 3921-3927.

16. X. Q. Yan, Z. Tang, J. J. Guo, C. Q. Jin, Y. Zhang, T. Goto, J. W. McCauley and M. W. Chen, *Phys. Rev. Lett.,* 2009, **102**, 075505/1-4.

17. K. M. Reddy, P. Liu, A. Hirata, T. Fujita and M. W. Chen, *Nature Comm.*, 2013, **4**, 2483/1-5.

18. S. Aryal, P. Rulis and W. Y. Ching, *Phys. Rev. B,* 2011, **84**, 184112/1-12.

19. Q. An, W. A. Goddard III and T. Cheng, *Phys. Rev. Lett.,* 2014, **113**, 095501/1-5.

20. http://libatoms.org

21. G. Kresse and J. Hafner, *Phys. Rev. B*, 1993, **47**, 558-561.

22. G. Kresse and J. Furthmuller, *Phys. Rev. B*, 1996, **54**, 11169-11186.

23. J. P. Perdew, K. Burke and M. Ernzerhof, *Phys. Rev. Lett.,* 1996, **77**, 3865-3868.

24. J. P. Perdew, K. Burke and M. Ernzerhof, *Phys. Rev. Lett.,* 1997, **78**, 1396.

25. P. E. Blochl, *Phys. Rev. B*, 1994, **50**, 17953-17979.

26. G. Kresse and D. Joubert, *Phys. Rev. B*, 1999, **59**, 1758-1775.

27. N. C. Halder and C. N. J. Wagner, *Acta Crystal.,* 1966, **20**, 312-313.

28. M. P. Seah, L. S. Gilmore and G. Beamson, *Surf. Interface Anal.,* 1998, **26**, 642-649.

29. J. H. Scofield, *J. Electron Spectrosc. Relat. Phenom.,* 1976, **8**, 129-137.

30. A. Jablonski and C. J. Powell, *Surf. Sci. Rep.,* 2002, **47**, 35-91.

31. S. Tanuma, C. J. Powell and D. R. Penn, *Surf. Interface Anal.,* 1994, **21**, 165-176.

32. G. Will, *"Die Kristallstruktur von C4AlB24"*, 1969, **25**, 1219; G. A. Meerson, S. S. Kiparisov, M. A. Gurevich, and F. Teng, *Poroshk. Metall.* (Kiev), 1965, **5**, 62; E. Gugel, R. Kieffer, G. Leimer, and P. Ettmayer, *Solid State Chem.*, 1972, **364**, 505; P. Dorner. Ph.D. Thesis, Universitat Stuttgart, Germany, (1982), (German); B. Morosin, T. L. Aselage and R. S. Feigelson, *Mater. Res. Soc. Symp. Proc.,* 1987, **97**, 145; R. Telle, NATO ASI Series, Ser E; Applied Sciences, 1990, **185**, 249; H. J. Seifert and F. Aldinger, *Struct. Bonding* (berlin, Ger.), 2002, **101**, 1; S. Hayun, N. Frage and M. P. Dariel, *J. Solid State Chem.*, 2006, **179**(9), 2875-2879; S. Hayun, A. Weizmann, M. P. Dariel and N. Frage, *J. Europ. Ceram. Soc.,* 2010, **30**(4), 1007-1014; S. Hayun, H. Dilman, M. P. Dariel and N. Frage, *Mater. Chem. Phys.,* 2009, **118**(203), 490-495; S. Hayun, V. Paris, M. P. Dariel, N. Frage and E. Zaretzky, *J. Eur. Ceram. Soc.,* 2009, **29**, 3395-3400; S. Hayun, M. P. Dariel and N. Frage, *Ceramic Transactions* 209 (Advances in Sintering Science and Technology), Publisher: American Ceramic Society, 2010, *209*, 29-41; S. Hayun, M. P. Dariel, N. Frage and E. Zaretsky, *Acta Materialia*, 2010, **58**(5), 1721-1732; S. Hayun, A. Weizmann, H. Dilman, M. P. Dariel and N. Frage, *J. Phys.: Conference Series*, 2009, **176**, 012009, doi:10.1088/1742-6596/176/1/012009.

33. R. Telle, *The Physics and Chemistry of Carbides, Nitrides and Borides*, NATO ASI Series, 1990, **185**, 249-267.

34. M. L. Trudeau, R. Schulz, D. Dussault, and A. Van Neste, *Phys. Rev. Lett.,* 1990, **64**(1), 99-102; Y-S. Kwon, K. B. Gerasimov, and S-K. Yoon, *J. Alloys and Compounds*, 2002, **346**, 276-281; Y-S. Kwon, J. S. Kim, I. V. Povstugar, E. P. Yelsukov, and P. P. Choi, *Phys. Rev. B*, 2007, **75**, 144112/1-6.

35. H. K. Clark and J. L. Hoard, *J. Am. Chem. Soc.,* 1943, **65**, 2115-2119.

36. A. C. Larson, *Amer. Inst. Phys. Conf. Proc.,* 1986, **140**, 109-112.

37. M. M. Balakrishnarajan, P. D. Pancharatna and R. Hoffmann, *New J. Chem.,* 2007, **31**, 473-485.

38. V.I. Matkovich, *J. Am. Chem. Soc.,* 1960, **83**, 1804-1806.

39. K. Shirai and S. Emura, *J. Phys. Condens. Mat.,* 1996, **8**, 10919-10929.

40.V. Domnich, Y. Gogotsi, M. Trenary and T. Tanaka, *Appl. Phys. Lett.,* 2002, **81(20)**, 3783-3785.

41. D. R. Tallant, T. L. Aselage, A. N. Campbell and D. Emin, *Phys. Rev. B: Condens. Matter,* 1989**, 40(8)**, 5649-5656.

42. J. Guo, L. Zhang, T. Fujita, T. Goto and M. Chen, *Phys. Rev. B: Condens. Matter Mater. Phys.,* 2010**, 81**, 060102/1-060102/4.

43. F. J. Bezares, J. P. Long, O. J. Glembocki, J. Guo, R. W. Rendell, R. Kasica, L. Shirey, J. C. Owrutsky and J. D. Caldwell, *Opt. Express,* 2013**, 21**, 27587-27601.

44. G. Subhash, D. Ghosh, J. Blaber, J. Q. Zheng, V. Halls and K. Masters, *Acta Mater.,* 2013**, 61**, 3888-3896.

45. D. Simeone, C. Mallet, P. Dubuisson, G. Baldinozzi, C. Gervais and J. Maquet, *J. Nucl. Mat.*, 2000, **277**, 1-10.

46. F. Mauri, N. Vast and C. J. Pickard, *Phys. Rev. Lett.,* 2001, **87**, 085506/1-4.

47.T. Harazono, Y. Hiroyama and T. Watanabe, *Bull. Chem. Soc. Jpn.,* 1996, **69**, 2419-2423.

48. T. M. Duncan, *J. Am. Chem. Soc.,* 1984**, 106**, 2270-2275.

49. K. Wade, in *Advances in Inorganic Chemistry and Radiochemistry*, H. J. Emeleus and A. G. Sharpe (eds.), Academic Press, 1976, **18**, pp 1-66.

50. W-Y. Dong, Y-J. Sun, H-Y. He and Y-C. Long, *Microporous and Mesoporous Materials*, 1999, **32**, 93–100.

51. R. J. Kirkpatrick, T. Aselage, B. L. Phillips and B. Montez, in *Proceedings of the Conference on Boron Rich Solids,* AIP Conf. Proc. No. 231 (AIP, New York, 1991), p. 261.

52. M. G. Kakazey, J. G. Gonzalez-Rodriguez, M. V. Vlasova and B. D. Shanina, *J. Appl. Phys.,* 2002**, 91**, 4438-4446.

53. J. W. Aptekar, M. C. Cassidy, A. C. Johnson, R. A. Barton, M. Lee, A. C. Ogier, C. Vo, M. N. Anahtar, Y. Ren, S. N. Bhatia, C. Ramanathan, D. G. Cory, A. L. Hill, R. W. Mair, M. S. Rosen, R. L. Walsworth and C. M. Macus, *ACS Nano,* 2009, **3***, 4003-4008.

54. J. Yamauchi, Y. Yoshimoto and Y. Suwa, *Appl. Phys. Lett.,* 2011, **99**(19), 191901/1-3.

55. M. Chen, J. W. McCauley, J. C. LaSalvia and K. J. Hemker, *J. Am. Cer. Soc.,* 2005, **88**(7), 1935-1942.

56. N. Nakata and A. Sekiguchi, *J. Am. Chem. Soc.,* 2006**, 128**, 422-423.

Table of Contents (TOC) entry
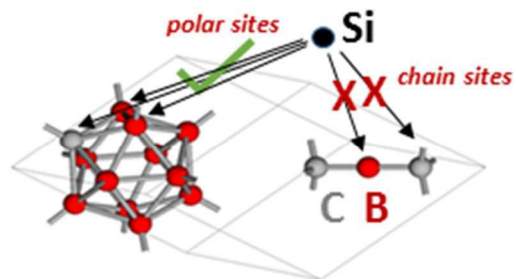
Substitution of silicon within the rhombohedral boron carbide (B_4C) crystal lattice at moderate temperatures (~200-400 ^{o}C) achieved through high-energy ball-milling